RSC Advances

PAPER

View Article Online
View Journal | View Issue

Cite this: *RSC Adv.*, 2019, **9**, 23029

Enhanced thermoelectric properties of Bi_2S_3 polycrystals through an electroless nickel plating process

Yi Chang, Qiong-Lian Yang, Jun Guo, Jing Feng and Zhen-Hua Ge *

Received 21st June 2019
Accepted 19th July 2019

DOI: 10.1039/c9ra04653d

rsc.li/rsc-advances

Bi_2S_3 is an eco-friendly alternative compound for thermoelectric devices. However, the low electrical conductivity of the pristine Bi_2S_3 hinders the improvement of its *ZT* value, which further restricts its application in the field of thermoelectricity. In this work, we report the first attempt to optimize the thermoelectric properties of Bi_2S_3 by electroless nickel plating. A nickel plated Bi_2S_3 powder sample was synthesized by electroless nickel plating on the precursor Bi_2S_3 powder prepared by mechanical alloying. Then, the powder was sintered to a bulk material by spark plasma sintering. The relationships between the composition, microstructure and thermoelectric properties of the bulk samples were investigated. The XRD results showed a $AgBi_3S_5$ second phase which was formed by the reaction of Ag residues with the Bi_2S_3 substrate during the sintering process. The nickel element and $AgBi_3S_5$ second phase introduced in the nickel plating process directly affect the electronic conductivity and Seebeck coefficient of the nickel plating sample, resulting in the relatively high power factor of 244 $\mu W\ m^{-1}\ K^{-2}$ at 628 K. What's more, the thermal conductivity of the sample was also reduced moderately, obtaining a low value of 0.40 $\mu W\ m^{-1}\ K^{-1}$ at 628 K. Therefore, a maximum *ZT* value of 0.38 was obtained at 628 K for the nickel plated sample, which is three times higher than that (0.12 at 628 K) of pristine Bi_2S_3 materials.

Introduction

In the past decades, thermoelectric materials have drawn worldwide scientific attention due to the fact that they could be capable of directly and reversibly converting heat energy into electrical power and provide an alternative for power generation and refrigeration.[1,2] Generally, the conversion efficiency of thermoelectric materials is dominated by the dimensionless thermoelectric figure of merit $ZT = (S^2\sigma/\kappa)T$, where S, σ, κ and T are Seebeck coefficient, electrical conductivity, thermal conductivity and the absolute temperature, respectively. Because of the well-known interrelated individual parameters, it is indeed a challenge to separately tune the S, σ and κ for the substantial improvement of the *ZT* value.[3–5] Several effective strategies, including band engineering, nanostructuring and nanoscopic approaches,[6–12] or intrinsically low thermal conductivity[13–15] have been successfully introduced and developed to improve the thermoelectric performance.

Despite achieving significant advances in this field, the state-of-the-art thermoelectric materials, including Bi_2Te_3,[10,16–18] PbX (X = S, Se and Te),[12,19,20] skutterudite,[21] half-Heusler and SiGe,[22–24] contain the rare and expensive elements such as Te and Hf, or toxic elements such as Pb and Sb, which have restricted their applications to niche markets. In order to make further large-scale application, new robust candidates, mainly comprised of non-toxic, inexpensive and earth-abundant elements, are urgent to be discovered and optimized.[25–27]

Compared with tellurium element, sulfur is more abundant in the earth, therefore, sulfur-based thermoelectric materials have received extensive attention such as PbS,[28,29] CoSbS,[30] Cu_2S,[31] SnS,[32] $CuFeS_2$,[33] *etc.* Among them, Bi_2S_3 is a typical V–VI thermoelectric materials with the band gap E_g of 1.3 eV. Bi_2S_3 has a high Seebeck coefficient and a relatively low thermal conductivity but its low electrical conductivity has resulted in a very low *ZT* value of 0.05 near the room temperature,[34] which is much lower than that of Bi_2Te_3. There is no doubt that improving the electrical conductivity of Bi_2S_3 material is the inevitable way for enhancing its thermoelectric property. Mostly recently, some researchers have reported that it is possible to enhance the electrical properties of the pristine Bi_2S_3. For example, Zhao *et al.* reported that sulfur vacancies can improve the electrical transport of Bi_2S_3.[35] Selenium incorporation in $Bi_2S_{3-x}Se_x$ solid solution triggered a 2.5-fold increase in the electrical conductivity of Bi_2S_3 nanowires.[36] The copper as electron donor in the layered Bi_2SeS_2-based alloys optimized the band structure and increased the carrier concentration, simultaneously nano-scale Bi_2S_3 precipitates enhance the phonon scattering.[37] Furthermore, the substitutions of silver,[38,39] copper,[40,41] antimony[42] and lanthanum[43] for bismuth sites, and selenium[44] for sulfur sites have also been investigated to increase the carrier concentration and electrical properties of

Faculty of Materials Science and Engineering, Kunming University of Science and Technology, Kunming, 650093, China. E-mail: zge@kmust.edu.cn

Bi_2S_3. It is well known that nickel has a good electrical conductivity, and electroless nickel plating is a mature process that can deposit nickel element uniformly on any substrate. At the best knowledge of us, there has no report about plating nickel on Bi_2S_3 materials. Therefore, in this work, the effect of nickel plating on the thermoelectric properties of Bi_2S_3 thermoelectric materials has been preliminarily investigated. For convenience, nickel plated bismuth sulfide material is referred to as BS@Ni. The bulk of BS@Ni materials obtained the maximum value of figure of the merit as 0.38 at 623 K, which was three times higher than that of untreated Bi_2S_3 materials. This shows that electroless nickel plating is a valuable method to optimize the thermoelectric properties, which is worthy of further studying.

Experimental section

In a typical experiment, to synthesis the Bi_2S_3 precursor powders, commercial purity powders of Bi (99.9%), S (99.95%) under the same 200 mesh were used as raw materials. The powders weighed with a chemical formula Bi_2S_3 were milled at 425 rpm for 12 h in a mixed atmosphere of high-purity argon (95%) and hydrogen (5%), using a planetary ball mill (QM-1SP2, Nanjing University, China). Stainless steel vessels and balls were used, and the weight ratio of the ball to powder was kept at 20 : 1. After that, the Bi_2S_3 precursor powder was mixed in a 30 ml aqueous solution of 0.75 g $SnCl_2$ (98%) and 1.2 ml HCl (36–38%) and stirred for 5 min to sensitize the Bi_2S_3 precursor powder. Then, after removing the sensitized solution, and the powder was placed in a 30 ml aqueous solution with 0.048 g $AgNO_3$ (99.8%) and stirred for 20 minutes to activate it. And further, allergic and activated Bi_2S_3 powder was placed in nickel plating solution with a PH value at 9 and stirred for 1.5 h in a 60 °C water bath. Finally, we obtained the nickel plated Bi_2S_3 after separating the supernatant and drying the mixture at 80 °C for 6 h. Nickel plating solution was prepared by successively mixing 30 ml aqueous solution with 4 g $NiSO_4 \cdot 6H_2O$ (98%), 6 g $Na_3C_6H_5O_7 \cdot 2H_2O$ (98%), 5.4 g $NaH_2PO_2 \cdot H_2O$ (99%) and 110 ml aqueous solution with 5 g HBO_3 (≥99.5%). The BS@Ni powder was charged into column graphite dies with 15 mm in internal diameter and then sintered in a vacuum using a SPS system (FDC SPS6321X, Japan) under 50 MPa at 773 K for 5 min. The sintered bulk samples were disks with a dimension of Φ 15 mm.

The phase structures of powder and bulk of BS@Ni were analyzed by X-ray diffraction (XRD, MiniFlex 600, Japan) with a CuKα radiation. The morphologies and elementary composition of powder and bulk of BS@Ni were characterized by the scanning electron microscopy and the energy dispersive spectrometer (SEM, EDS, EVO18, Germany). The TE properties were evaluated along the sample section which is perpendicular to the pressing direction of SPS. The Seebeck coefficient and electrical resistivity were measured form 323 K to 673 K in helium atmosphere using a Seebeck coefficient/electrical resistance measuring system (ZEM-3, Ulvac-Riko, Japan). The density of the sample was measured by the Archimedes method. The thermal conductivity of the sample was calculated by the relationship of $\kappa = DC_P\rho$ from the thermal diffusivity (D) measured by the laser flash method (NETZSCH, LFA457, Germany), specific heat capacity (C_P) and density (ρ).

Result and discussion

Fig. 1 show XRD patterns and the main peak enlargement patterns of Bi_2S_3 and BS@Ni powders and bulks. The standard diffraction patterns of Bi_2S_3 (PDF# 17-0320) and $AgBi_3S_3$ (PDF# 50-1645) cited from the database are also plotted in Fig. 1(a) for comparison. Most of diffraction peaks can be indexed to the standard diffraction patterns of Bi_2S_3, but a second phase of $AgBi_3S_5$ was detected in the XRD patterns of BS@Ni bulk sample. The second phase may be produced by the reaction between the residual Ag element from activation process and Bi_2S_3 materials during the sintering process. The effect of the second phase on the thermoelectric performance of Bi_2S_3 bulk sample will be discussed later. In the Fig. 1(b), the XRD patterns of the bulk part are obviously shifted to the low angle compared with that of the powder parts, and the full widths of half maximum are reduced, indicating that crystallization process occurred in the process of SPS sintering, which led the increase of grain size. Furthermore, the BS@Ni sample produce a greater shift of the (130) diffraction peaks to lower angle, indicating that the nickel elements entered into the interstitial site of the Bi_2S_3 matrix and increased the crystal plane distance. Meanwhile, the XRD pattern of the powder of BS@Ni sample is also obviously shifted to the low angle compared with that of pure Bi_2S_3 phase because of the addition of Ni and Ag elements, but no significant second phase is detected.

The morphologies of Bi_2S_3 and BS@Ni powders are shown in Fig. 2(a) and (b). The morphologies of the powders before and after nickel plating are almost the same, which are consisted of different particles whose sizes ranging from 0.3 μm to 2 μm. Furthermore, Fig. 2(c) and (d) show the face element scanning results from the area of Fig. 2(a) and (b). As shown in the figures, the ratio of Bi content to S content in the pristine Bi_2S_3 powder is 39.60 to 60.40, which is close to the stoichiometry ratio of 2 : 3. On the other hand, the ratio of Bi to S of the BS@Ni powder is 38.68 to 58.79, which is the same as the ratio of pristine Bi_2S_3 powder. It indicates that the composition of Bi_2S_3 did not change during the nickel plating process. In addition, the content of Ag and Ni is only about 1.29% and 1.23% respectively. Combined with nickel plating process, we believe that due to the small size of micron-scale of powders, it is difficult to conduct coarsening or hydrophilic treatment, resulting in a difficult formation of Ag catalytic nucleation center in the activation process. Meanwhile, part of the catalytic nucleation center of Ag element failed to reduce Ni ions, so that the final powder contained only a small amount of Ni element and a small amount of residual Ag element. It is precisely because of the low contents of these two elements that the diffraction peaks cannot be observed in the XRD patterns.

After sintering, the morphologies and mapping results of elements distribution of Bi_2S_3 and BS@Ni bulks are shown in Fig. 3. The morphology of Bi_2S_3 sintered block is relatively dense, which is consistent with the experimental result that the relative density of Bi_2S_3 bulk is 97.5%. In contrast, the relative

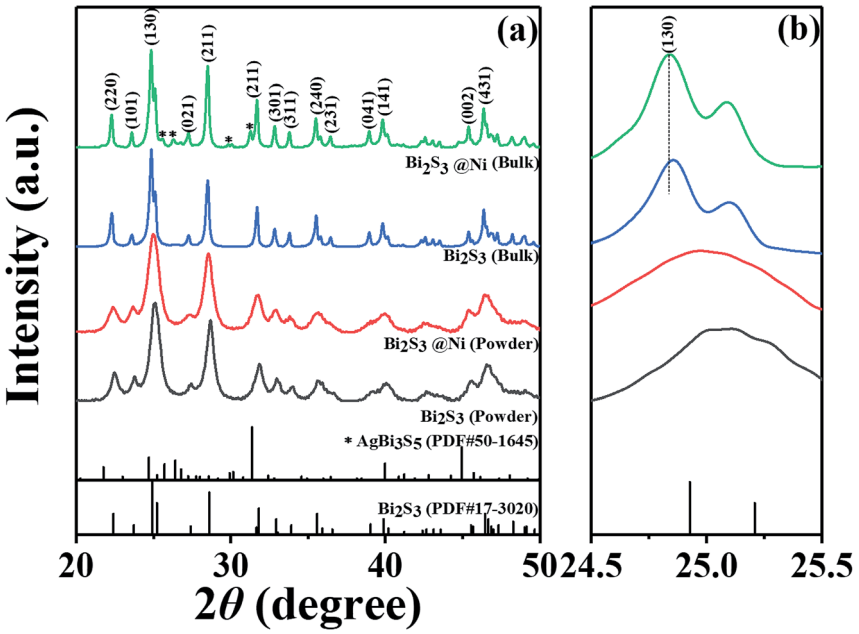

Fig. 1 XRD patterns and the main peak enlargement patterns of Bi_2S_3 and BS@Ni powders and bulks. (a) XRD patterns of Bi_2S_3 and BS@Ni powders and bulks. (b) Main peak enlargement patterns of Bi_2S_3 and BS@Ni powders and bulks.

density of BS@Ni is only 85%. As shown in Fig. 3(b), more pores in the BS@Ni bulk lead to its lower relative density. Combined with the XRD results of nickel plated block in Fig. 1(a), more pores in the morphology may be due to the fact that the silver particles which are on the surface of the powder reacted with the Bi_2S_3 substrate during the sintering process and generating $AgBi_3S_5$. It leads to the instability of the structure. The unstable structure leads to the loss of sulfur and generating more pores further. In addition, we also observe obvious layered structure in Fig. 3(b). What's more, the face scanning results of elements distribution are shown in the Fig. 3(c)–(f) respectively. As shown in Fig. 3(d), More Ni elements are distributed at the edge of Bi_2S_3 substrate but the distribution of Ag elements is relatively uniform, and there are partial distributions within the bulk in

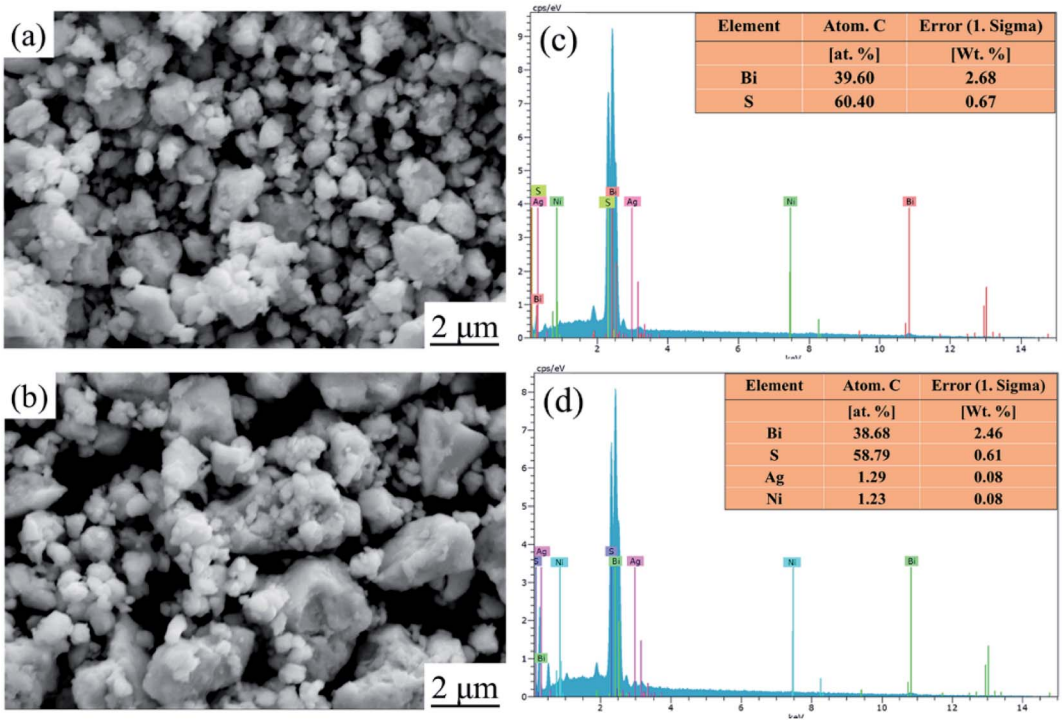

Fig. 2 SEM images and face scanning results of element contents of Bi_2S_3 and BS@Ni powders. (a) SEM image of Bi_2S_3 powder, (b) SEM image of BS@Ni powder, (c) face element scanning result of Bi_2S_3 powder from (a), (d) face element scanning result of BS@Ni powder from (b).

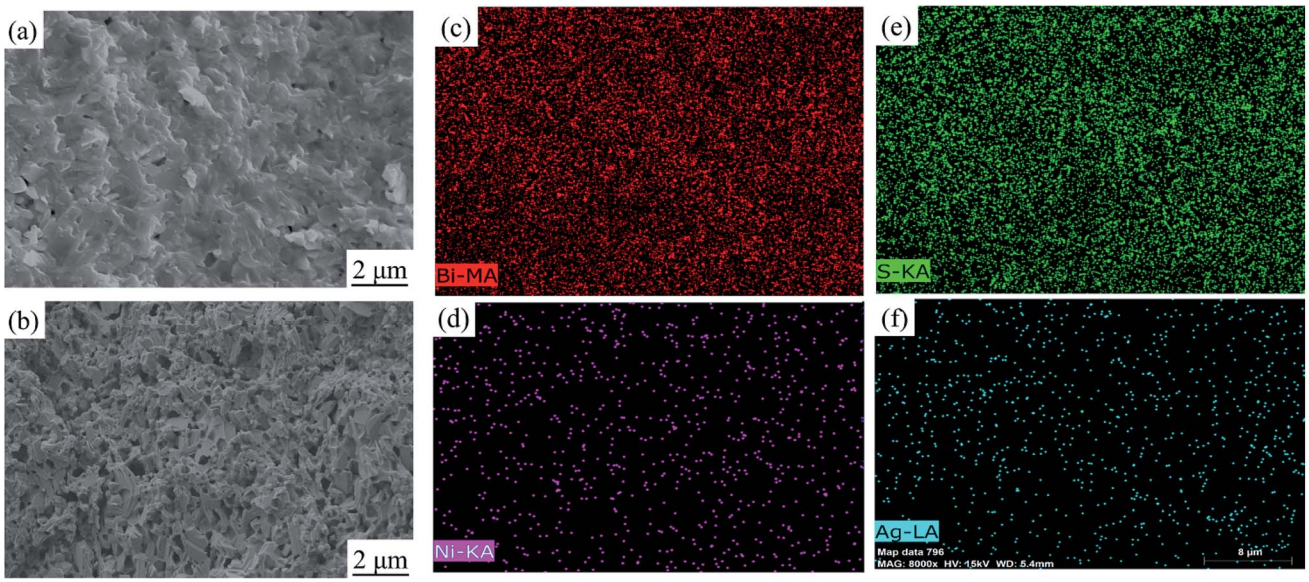

Fig. 3 SEM images and face scanning results of element distribution of Bi_2S_3 and BS@Ni bulks. (a) SEM image of Bi_2S_3 bulk, (b) SEM image of BS@Ni bulk, (c) the Bi element distribution result of BS@Ni bulk, (d) the Ni element distribution result of BS@Ni bulk, (e) the S element distribution result of BS@Ni bulk, (f) the Ag element distribution result of BS@Ni bulk.

Fig. 3(f). The reason for this phenomenon may be that, in the recrystallization process of sintering, the theory of crystal growth kinetics shows that the Bi_2S_3 with layered structure is more likely to grow along the surface steps. The steps are also easy places to deposit Ni or Ag. Therefore, the Ni elements deposited on the surface of the substrate are continuously shifted to the boundary position as the crystal grows but the Ag elements reacted with the matrix and therefore obtaining a relatively uniform distribution. Finally, the result of element distribution is shown in Fig. 3(d) and (f). In order to facilitate the understanding, the process of nickel plating on bismuth sulfide powders and the element distribution in the sintered BS@Ni bulk are made into a schematic diagram, which is drawn in the Fig. 4.

Further, the thermoelectric properties of Bi_2S_3 and Bi_2S_3@Ni bulks are shown in the Fig. 5. Among them, the errors of electrical properties are 3%, the errors of thermal properties are 5%, and the error of ZT value is 20%. Fig. 5(a) show the temperature-dependent electrical conductivities of Bi_2S_3 and BS@Ni bulks. The curves of electrical conductivity as a function of temperature exhibit distinct difference. The electrical conductivity of pristine Bi_2S_3 increases gradually with temperature rising, showing typical semiconductor behavior. At 628 K, the value of electrical conductivity of pristine Bi_2S_3 is only about 7.153 S cm^{-1}. For the BS@Ni sample, the electrical conductivity monotonously decreases with the temperature increasing, showing typical strong degenerate semiconductor behavior. In numerical aspect, the value of electrical conductivity of BS@Ni sample decrease form 38.4 S cm^{-1} at 334 K to 28.9 S cm^{-1} at 628 K. The lowest value is four times that of the conductivity of the original Bi_2S_3 at the same temperature. This is because the second phase of $AgBi_3S_5$ with high conductivity (which is about 42 S cm^{-1}) was produced during the preparation of nickel plated samples. The incorporation of the second phase and Ni

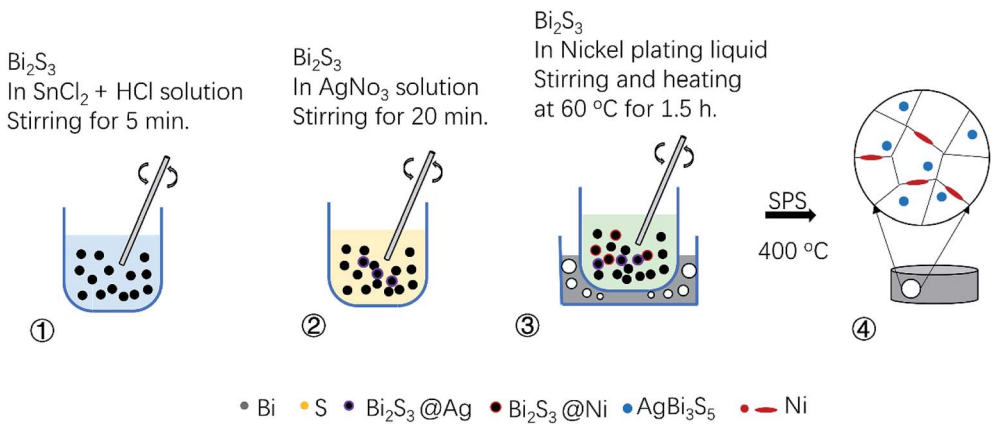

Fig. 4 Schematic diagram of nickel plating process and element distribution of BS@Ni bulk.

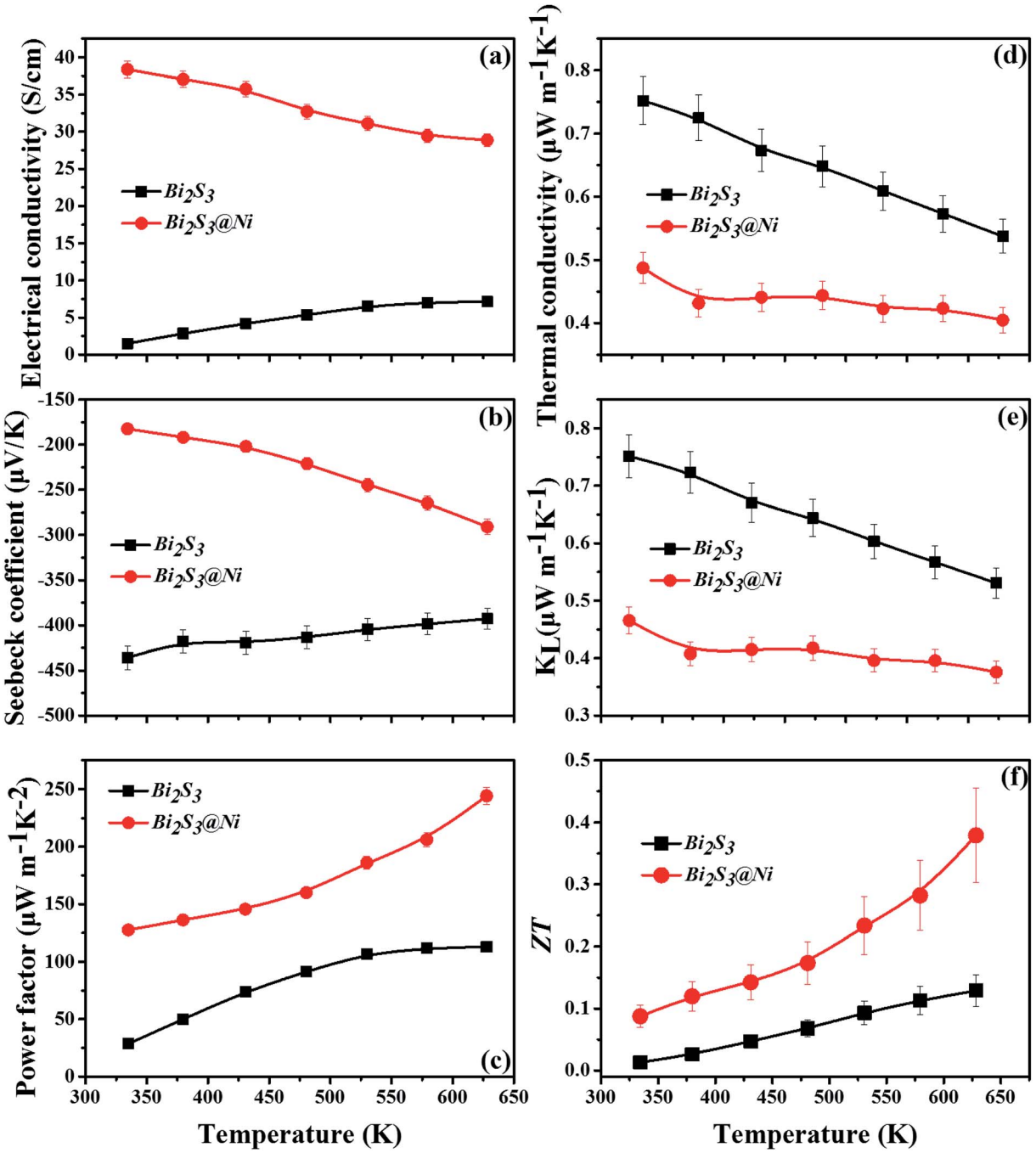

Fig. 5 Thermoelectrical properties of Bi_2S_3 sample and BS@Ni sample. (a) Electrical conductivity, (b) Seebeck coefficient, (c) power factor, (d) thermal conductivity, (e) lattice thermal conductivity, (f) ZT.

elements resulted in the increase of S vacancies in the lattice and the enhancement of carrier concentration. At the same time, the Ni element distributing at the boundary position also improved the carrier mobility, so that the conductivity of the BS@Ni sample did not drop significantly with the increase of temperature as reported by Tan *et al.*,[45] and the value remained four times that of the pristine bismuth sulfide.

The temperature-dependent Seebeck coefficients of pristine Bi_2S_3 and BS@Ni sample are plotted in Fig. 5(b). All the samples show negative coefficient value in the whole measuring temperature range, indicating n-type semiconductors. For the pristine bismuth sulfide sample, the absolute value of Seebeck coefficient decreased with the increase of temperature. According to equation $S = \frac{8\pi^2 {K_B}^2}{3eh^2} m^* T \left(\frac{\pi}{3n}\right)^{2/3}$, it is clear that the Seebeck coefficient is positively proportionate to the electron effective mass (m^*) at Fermi level and negatively to the carrier concentration (n). Therefore, the absolute value of Seebeck coefficient of the pristine Bi_2S_3 sample decreases gradually with the increase of carrier concentration caused by intrinsic

excitation with the temperature increasing. Also affected by the intrinsic excitation of BS@Ni sample, the absolute value of Seebeck coefficient of BS@Ni sample increases gradually with the temperature rising. For BS@Ni sample, the hole carriers induced by intrinsic excitation have a more obvious cancellation effect on most electron carriers, which makes the carrier concentration decrease with the increase of temperature, resulting in the increase of absolute value of Seebeck coefficient. Also limited by the high carrier mobility, the absolute value of Seebeck coefficient of BS@Ni sample did not reach the level of the pristine Bi_2S_3 sample, and the maximum value was 291 μV K^{-1} at 628 K.

Fig. 5(c) shows the temperature-dependent power factors of pristine Bi_2S_3 and BS@Ni samples, which are calculated from the formula $PF = \alpha|S|^2$, where α is electrical conductivity and S is Seebeck coefficient, respectively. As shown in the Fig. 5(c), PF of the BS@Ni samples is much higher than that of the pristine Bi_2S_3 sample at all temperature range due to the enhanced electrical transport properties by Ni plating. The peak value of 244 μW m^{-1} K^{-2} at 628 K for BS@Ni samples was two times higher than that of pristine Bi_2S_3 sample at the same temperature.

In usual, we will write the total thermal conductivity κ_{total} of solids as follows:

$$\kappa_{total} = \kappa_{lat} + \kappa_{el}, \quad (1)$$

where κ_{lat} is the lattice contribution and κ_{el} is the electronic contribution. κ_{el} can be calculated using the Wiedemann–Franz–Lorenz relation:

$$\kappa_{el} = L\sigma T, \quad (2)$$

where L is the Lorenz number, σ is the electrical conductivity, and T is the absolute temperature. Reduced Fermi energy was used to calculate Lorenz number (L) (eqn (3)) varies as Seebeck value changes (eqn (4)) with temperature or composition. The L calculation was estimated in a traditional single parabolic band model (resulting in an L with a deviation of less than 10% as compared with a more rigorous single non-parabolic band and multiple band models calculation), where the reduced Fermi energy was implicitly determined by the Seebeck values (eqn (4)). When the κ_{el} is calculated, the κ_{lat} is obtained by subtracting it from the κ_{total}.

$$L = \left(\frac{k_B}{e}\right)^2 \left(\frac{(r+7/2)F_{r+5/2}(\eta)}{(r+3/2)F_{r+1/2}(\eta)} - \left[\frac{(r+5/2)F_{r+3/2}(\eta)}{(r+3/2)F_{r+1/2}(\eta)}\right]^2\right), \quad (3)$$

$$S = \pm\frac{k_B}{e}\left[\frac{(r+5/2)F_{r+3/2}(\eta)}{(r+3/2)F_{r+1/2}(\eta)} - \eta\right], \quad (4)$$

Variations of the κ_{total} and κ_{lat} of Bi_2S_3 sample and BS@Ni sample with temperature are shown in Fig. 5(d) and (e). As shown in Fig. 5(d), the κ_{total} of BS@Ni sample is obviously lower than that of the pristine Bi_2S_3 sample. With the increase of temperature, the κ_{total} of BS@Ni samples gradually decreased from 0.48 W m^{-1} K^{-1} at room temperature to 0.40 W m^{-1} K^{-1} at 628 K, this was significantly lower than the 0.54 W m^{-1} K^{-1} of the pristine Bi_2S_3 sample at 628 K. This indicates that nickel plating is an effective method to reduce the κ_{total} of Bi_2S_3 materials. By comparing the values of κ_{total} and κ_{lat} in Fig. 5(d) and (e), it is not difficult to find that the κ_{lat} is dominant in the κ_{total} composition of the two samples. Compared with the pristine Bi_2S_3 sample, the κ_{lat} of BS@Ni sample decreased obviously. This indicates that the introduction of the second phase and the Ni element by the nickel plating process increased the scattering of phonons, resulting in the reduction of the κ_{lat} of the BS@Ni sample, and then led to a significant decrease in the κ_{total} of the BS@Ni sample.

The curves of ZT value of pristine Bi_2S_3 sample and BS@Ni sample are plotted in the Fig. 5(f). The ZT value of the BS@Ni sample is significantly higher than that of the pristine Bi_2S_3 sample due to the increased conductivity and decreased conductivity by nickel plating process. Its ZT value reaches the maximum value of 0.38 at 628 K, which is three times higher than that of pristine Bi_2S_3 materials. This proves that nickel plating is an effective method to optimize the thermoelectric properties of Bi_2S_3 materials.

Conclusion

In this work, BS@Ni samples was synthesized by electroless nickel plating on the mechanical alloying precursor-Bi_2S_3 powder and further spark plasma sintering. Its composition, microstructure, electrical and thermal transport properties have been investigated. Due to the influence of matrix particle size, the content of coating Ni elements are less, and there are a small amount of residual Ag elements. In the sintering process, residual Ag elements reacted with the base Bi_2S_3 material and formed $AgBi_3S_5$ second phase. The nickel element and $AgBi_3S_5$ second phase which introduced in the nickel plating process led to the increase of carrier concentration and mobility, resulting in significantly improvement of the electrical conductivity of BS@Ni sample. Meanwhile the Seebeck coefficient of BS@Ni sample still remained relatively high values of over 180 μV K^{-1} in the whole measuring temperature range. Therefore, the BS@Ni sample obtained a relatively high power factor of 244 μW m^{-1} K^{-2} at 628 K. Combined with a low thermal conductivity value of 0.40 W m^{-1} K^{-1} at 628 K, a maximum ZT value of 0.38 was obtained, which is three times higher than that of pristine Bi_2S_3 materials ($ZT = 0.12$). Therefore, nickel plating is an effective method to optimize the thermoelectric properties of Bi_2S_3 materials.

Conflicts of interest

There are no conflicts to declare.

Acknowledgements

This work was supported by the National Natural Science Foundation of China (Grant No. 11764025).

References

1 *CRC Handbook of Thermoelectrics*, ed. D. M. Rowe, 1995.
2 J. Yang and T. Caillat, *MRS Bull.*, 2006, **31**, 224.
3 G. J. Snyder and E. S. Toberer, *Nat. Mater.*, 2008, **7**, 105.
4 M. Zebarjadi, K. Esfarjani, M. S. Dresselhaus, Z. F. Ren and G. Chen, *Energy Environ. Sci.*, 2012, **5**, 5147.
5 J. R. Sootsman, D. Y. Chung and M. G. Kanatzidis, *Angew. Chem., Int. Ed.*, 2009, **48**, 8616.
6 Y. Z. Pei, H. Wang and G. J. Snyder, *Adv. Mater.*, 2012, **24**, 6125.
7 J. P. Heremans, V. Jovovic, E. S. Toberer, A. Saramat, K. Kurosaki, A. Charoenphakdee, S. Yamanaka and G. J. Snyder, *Science*, 2008, **321**, 554.
8 Y. Z. Pei, X. Y. Shi, A. Lalonde, H. Wang, L. D. Chen and G. J. Snyder, *Nature*, 2011, **473**, 66.
9 W. S. Liu, X. Yan, G. Chen and Z. F. Ren, *Nano Energy*, 2012, **1**, 42.
10 B. Poudel, Q. Hao, Y. Ma, Y. C. Lan, A. Minnich, B. Yu, X. A. Yan, D. Z. Wang, A. Muto, D. Vashaee, X. Y. Chen, J. M. Liu, M. S. Dersselhaus, G. Chen and Z. F. Ren, *Science*, 2008, **320**, 634.
11 L. D. Zhao, V. P. Dravid and M. G. Kanatzidis, *Energy Environ. Sci.*, 2014, **7**, 251.
12 K. Biswas, J. Q. He, I. D. Blum, C. I. Wu, T. P. Hogan, D. N. Seidman, V. P. Dravid and M. G. Kanatzidis, *Nature*, 2012, **489**, 414.
13 L. D. Zhao, S. H. Lo, Y. Zhang, H. Sun, G. Tan, C. Uher, C. Wolveton, V. P. Dravid and M. G. Kanatzidis, *Nature*, 2014, **508**, 373.
14 L. D. Zhao, D. Berardan, Y. L. Pei, C. Byl, L. Pinsard-Gaudart and N. Dragoe, *Appl. Phys. Lett.*, 2010, **97**, 092118.
15 M. D. Nielsen, V. Ozolins and J. P. Heremans, *Energy Environ. Sci.*, 2013, **6**, 570.
16 X. Yan, B. Poudel, Y. Ma, W. S. Liu, G. joshi, H. Wang, Y. C. Lan, D. Z. Wang, G. Chen and Z. F. Ren, *Nano Lett.*, 2010, **10**, 3373.
17 W. S. Liu, Q. Y. Zhang, Y. C. Lan, S. Shuo, X. Yan, Q. Zhang, H. Wang, D. Z. Wang, G. Chen and Z. F. Ren, *Adv. Energy Mater.*, 2011, **1**, 577.
18 W. S. Liu, K. C. Lukas, K. McEnaney, S. Lee, Q. Zhang, C. P. Opeil, G. Chen and Z. F. Ren, *Energy Environ. Sci.*, 2013, **6**, 552–560.
19 L. D. Zhao, S. Q. Hao, S. H. Lo, C. I. Wu, X. Y. Zhou, Y. Lee, H. Li, K. Biswas, T. P. Hogan, C. Uher, C. Wolverton, V. P. Dravid and M. G. Kanatzidis, *J. Am. Chem. Soc.*, 2013, **135**, 7364.
20 L. D. Zhao, S. H. Lo, J. Q. He, H. Li, K. Biswas, J. Androulakis, C. I. Wu, T. P. Hogan, D. Y. Chung, V. P. Dravid and M. G. Kanatzidis, *J. Am. Chem. Soc.*, 2011, **133**, 20476.
21 X. Shi, J. Yang, J. R. Salvador, M. Chi, J. Y. Cho, H. Wang, S. Bai, J. Yang, W. Zhang and L. D. Chen, *J. Am. Chem. Soc.*, 2011, **133**, 7837.
22 S. Chen and Z. F. Ren, *Mater. Today*, 2013, **16**, 387.
23 G. Joshi, T. Dahal, S. Chen, H. Z. Wang, J. Shiomi, G. Chen and Z. F. Ren, *Nano Energy*, 2013, **2**, 82.
24 G. Joshi, H. Lee, Y. C. Lan, X. W. Wang, G. H. Zhu, D. Z. Wang, R. W. Gould, D. C. Cuff, M. Y. Tang, M. S. Dresselhaus, G. Chen and Z. F. Ren, *Nano Lett.*, 2008, **8**, 4670.
25 W. Liu, X. J. Tan, K. Yin, H. J. Liu, X. F. Tang, J. Shi, Q. J. Zhang and C. Uher, *Phys. Rev. Lett.*, 2012, **108**, 166601.
26 J. Li, J. H. Sui, Y. L. Pei, C. Barreteau, D. Berardan, N. Dragoe, J. Q. He and L. D. Zhao, *Energy Environ. Sci.*, 2012, **5**, 8543.
27 Y. He, T. Day, T. S. Zhang, H. L. Liu, X. Shi, L. D. Chen and G. J. Snyder, *Adv. Mater.*, 2014, **26**, 3974.
28 C. Chang, Y. Xiao, X. Zhang, Y. L. Pei, F. Li, S. L. Ma, B. F. Yuan, Y. Liu, S. K. Gong and L. D. Zhao, *J. Alloys Compd.*, 2016, **664**, 411–416.
29 S. Johnsen, J. Q. He, J. Androulakis, V. P. Dravid, L. Todorov, D. Y. Chung and M. G. Kanatzidis, *J. Am. Chem. Soc.*, 2011, **133**, 3460–3470.
30 W. Yao, D. F. Yang, Y. C. Yan, K. L. Peng, H. Zhang, A. P. Liu, X. Lu, G. Y. Wang and X. Y. Zhou, *ACS Appl. Mater. Interfaces*, 2017, **9**, 10595–10601.
31 Y. He, T. Day, T. S. Zhang, H. L. Liu, X. Shi, L. D. Chen and G. J. Snyder, *Adv. Mater.*, 2014, **26**, 3974–3978.
32 Q. Tan, L. D. Zhao, J. F. Li, C. F. Wu, T. R. Wei, Z. B. Xing and M. G. Kanatzidis, *J. Mater. Chem. A*, 2014, **2**, 17302.
33 J. H. Li, Q. Tan and J. F. Li, *J. Alloys Compd.*, 2013, **551**, 143–149.
34 B. X. Chen and C. Uher, *Chem. Mater.*, 1997, **9**, 1655–1658.
35 L. D. Zhao, B. P. Zhang, W. S. Liu, H. L. Zhang and J. F. Li, *J. Solid State Chem.*, 2008, **181**, 3278–3282.
36 A. A. Rahman, R. Huang and L. Whittaker-Brooks, *Chem. Mater.*, 2016, **28**, 6544–6552.
37 L. Li, Y. Liu, J. Y. Dai, H. X. Zhu, A. J. Hong, X. H. Zhou, Z. F. Ren and J. M. Liu, *Nano Energy*, 2015, **12**, 447–456.
38 Z. H. Ge, B. P. Zhang, Y. Q. Yu and P. P. Shang, *J. Alloys Compd.*, 2002, **514**, 205–209.
39 Y. Q. Yu, B. P. Zhang, Z. H. Ge, P. P. Shang and Y. X. Chen, *Mater. Chem. Phys.*, 2011, **131**, 216–222.
40 Z. H. Ge, B. P. Zhang, Y. Liu and J. F. Li, *Phys. Chem. Chem. Phys.*, 2012, **14**, 4475–4481.
41 V. Tarachand, R. Sharma, V. Bhatt and G. S. Ganesan, *Nano Res.*, 2016, **9**, 3291–3304.
42 Y. Kawamoto and H. Iwasaki, *J. Electron. Mater.*, 2014, **43**, 1475–1479.
43 F. Han, H. Liu, C. D. Malliakas, M. Sturza, D. Y. Chung, X. Wan and M. G. Kanatzidis, *Inorg. Chem.*, 2016, **55**, 3547–3552.
44 L. J. Zhang, B. P. Zhang, Z. H. Ge and C. G. Han, *Solid State Commun.*, 2013, **162**, 48–52.
45 G. Tan, S. Hao, J. Zhao, C. Wolverton and M. G. Kanatzidis, *J. Am. Chem. Soc.*, 2017, **139**, 6467–6473.